

# Nonlinear Development and Observational Consequences of Wardle C-Shock Instabilities

Mordecai-Mark Mac Low

Max-Planck-Institut für Astronomie, Königstuhl 17, D-69117 Heidelberg, Germany;  
mordecai@mpia-hd.mpg.de

and

Michael D. Smith

Astronomisches Institut der Universität Würzburg, Am Hubland, D-97074 Würzburg,  
Germany; smith@astro.uni-wuerzburg.de

ApJ, submitted, 26 March 1997

## ABSTRACT

We compute the nonlinear development of the instabilities in C-shocks first described by Wardle, using a version of the ZEUS code modified to include a semi-implicit treatment of ambipolar diffusion. We find that, in three dimensions, thin sheets parallel to the shock velocity and perpendicular to the magnetic field lines form. High resolution, two-dimensional models show that the sheets are confined by the Brandenburg & Zweibel ambipolar diffusion singularity, forcing them to numerically unresolvable thinness. Hot and cold regions form around these filaments, disrupting the uniform temperature structure characteristic of a steady-state C-shock. This filamentary region steadily grows as the shock progresses. We compare steady-state to unstable C-shocks, showing excitation diagrams, line ratios, and line profiles for molecular hydrogen lines visible in the K-band, with the *Infrared Space Observatory*, and with NICMOS on the *Hubble Space Telescope*.

*Subject headings:*

## 1. Introduction

Within molecular clouds, interstellar gas becomes dense enough to recombine almost completely, reaching levels of fractional ionization less than  $\chi = 10^{-4}$ . Positively charged ions or grains carry the magnetic field in most regions except the central portions of protostellar disks, where neutral number densities exceed  $10^{10} \text{ cm}^{-3}$  and electron-ion drift becomes important (*e.g.* Königl 1989). The charged particles carrying the field couple in turn with the neutral gas through collisions. When the fractional ionization is high, neutrals collide frequently with ions, and the field is coupled tightly to the neutrals. As the number of ions drops, they begin to resemble a sieve, and it becomes easier and easier for neutral gas to slip between adjacent ions, so that the field decouples from the neutral gas, diffusing through it. This process is called ambipolar diffusion, and was first understood to be astrophysically important by Mestel and Spitzer (1956) and Mouschovias (1979). In protostellar cores, ambipolar diffusion of the field out past infalling gas allows mass to fall in to the central region without dragging field along with it. In protostellar disks, ambipolar diffusion may allow the magnetic field to drive jets, reducing the angular momentum of accreting gas.

One of the most directly observable effects of ambipolar diffusion is to spread out shock waves in dense gas (Draine 1980). Normally, the thickness of shocks is determined by gas dynamical or MHD dissipation in the shock front. Typical jump or J-shocks in the interstellar medium have thicknesses much shorter than the cooling length of the gas, so immediately behind the shock front, the gas gets quite hot, reaching the post-shock temperature predicted by the shock jump conditions for adiabatic gas. On the other hand, if a shock wave moves faster than the sound speed,  $c_s$ , but slower than the Alfvén speed in the rarefied ions,  $v_{Ai} = |\mathbf{B}|^2 / \sqrt{4\pi\rho_i}$ , where  $\mathbf{B}$  is the magnetic field and  $\rho_i$  is the ion density, a compression wave can travel through the field and ions, moving faster than the neutral shock front. The accelerated ions can then accelerate the neutrals through collisional drag, spreading the shock front into a broad continuous shock, or C-shock, in which ambipolar diffusion maintains the thick shock front. C-shocks typically have thicknesses greater than the cooling length, so the gas cools as it is accelerated, and never reaches the high temperatures predicted for J-shocks. A recent review covering these points was written by Draine & McKee (1993).

C-shocks were shown to be unstable by Wardle (1990, 1991a,b). The mechanism depends on the field lines in a steady-state C-shock being perturbed so as to no longer be exactly perpendicular to the flow, as shown in Figure 1. The ions have low inertia and collide frequently with neutrals, so a drag force due to the component of the neutral velocity parallel to the perturbed field lines drives the ions along the field lines into the valleys and

away from the peaks of the field lines.

The density of ions in the valleys depends inversely on the wavelength of the perturbation for constant perturbation size, for two reasons. First, the ions have longer to travel to reach a valley at longer wavelengths, and second, the field lines are more normal to the flow at longer wavelengths, so the component of the neutral drag force driving ions into the valleys is lower. As the ions concentrate in the valleys, and rarefy at the peaks, the drag of the neutrals on the ions changes proportional to the ion density, transferring neutral momentum to the field, and producing a growing perturbation that leads in turn to more ion accumulation.

There are stabilizing forces at both long and short wavelengths that act against the perturbation, due to magnetic pressure and tension, respectively. At long wavelengths, magnetic pressure acts on field lines compressed into valleys by the increased drag forces there, slowing or preventing further growth. At short wavelengths, magnetic tension acts against the curvature of field lines in valleys and peaks caused by increasing perturbation size, again slowing or preventing further growth. As a result, there exists an intermediate wavelength of maximum growth, computed by Wardle (1990) in his linear analysis. In three dimensions, the fastest growing modes were found by Wardle to be slabs, with no variation in the third direction. If there were variation, the compressed magnetic fields in the valleys could twist out sideways into the third dimension, releasing magnetic pressure, but decreasing the drag forces acting along the field lines, and so slowing the growth of the instability.

Prior computations including ambipolar diffusion have focused on the collapse of protostellar cores and on the stability of C-shocks. The first dynamical computation to include ambipolar diffusion was done by Black & Scott (1982) using a two-dimensional, first-order code that included an iterative approximation to an implicit method of computing the ambipolar diffusion. Paleologou & Mouschovias (1983) described a one-dimensional code that included an adaptive mesh and an implicit method for the ambipolar diffusion. Fiedler & Mouschovias (1992) described a two-dimensional code with adaptive mesh and an implicit method. Mouschovias & Morton (1991) computed protostellar collapse problems by integrating over the vertical structure of an accretion disk and using an implicit method to model the horizontal, axisymmetric flow. Tóth (1994, 1995) used a two-dimensional, flux corrected transport code to investigate C-shock stability, using both explicit and implicit methods. Mac Low et al. (1995) added ambipolar diffusion to the ZEUS code<sup>1</sup>

---

<sup>1</sup>Available for community use by registration with the Laboratory for Computational Astrophysics at [lca@ncsa.uiuc.edu](mailto:lca@ncsa.uiuc.edu)

(Stone & Norman 1992a, b) and investigated its effects on Balbus-Hawley instabilities as a first application.

In this paper we examine the nonlinear evolution of the Wardle instability with high-resolution two-dimensional and three-dimensional computations, extending the work of Mac Low et al. (1995) by adding the ion mass conservation equation, and a semi-implicit treatment of the ion momentum equation, following Tóth (1995), in order to compute two- and three-dimensional models of unstable C-shocks. A preliminary version of this paper was presented by Mac Low & Smith (1997). Stone (1997) describes similar computations.

## 2. Scales and Parameters

The time and length scales for our problem are the time for material to flow through a C-shock (e.g., Tóth 1995; Wardle 1990), given by the time required for every neutral to collide with an ion  $t_{flow} = t_{ni} = 1/\gamma\rho_{i0}$ , where the variables are defined below, under equation (4); and the thickness of the C-shock, given by  $L_{shk} = \sqrt{2}v_{An}t_{flow}$ .

The time-dependent shock flow pattern is fully determined by four control parameters: the Alfvén number  $A_n$ , the Mach number  $M$ , the ion fraction and the initial field orientation. The Wardle instability is insensitive to the ion fraction and Mach number so long as they allow for the existence of a C-shock at all. Therefore only one parameter,  $A_n$ , is necessary to describe the whole class of transverse, low-ionisation, cold flows: a single flow simulation with a fixed Alfvén number is relevant to a wide range of conditions.

The time scales for ionization and recombination can be important as well. Specifically, if the recombination timescale is significantly shorter than the flow timescale, the possibility exists of the instability being suppressed. If the ions are primarily molecular ions such as  $\text{H}_3\text{O}^+$ , dissociative recombination rates may be high enough for this to be relevant (Flower & Pineau de Forêts, personal communication). We will only consider this case in the extreme limit of constant ion density, which we will show does indeed suppress the instability.

In this paper we discuss both two- and three-dimensional models. Our “standard model” has neutral Alfvén number  $A_n = (v_s/B_0)\sqrt{4\pi\rho_{n0}} = 25$ , initial number density of H atoms  $n_H = 10^5 \text{ cm}^{-3}$ , (note that  $\rho_n = 1.4n_H$ ), fractional ionization  $\chi = 10^{-4}$ , shock velocity  $v_s = 5 \text{ km s}^{-1}$ , sound speed  $c_s = 0.01 \text{ km s}^{-1}$ , ion mass  $m_i = 10m_H$ , and neutral mass  $m_n = 7/3m_H$ , assuming 10% He. We use an ion-neutral collisional coupling constant  $\gamma = \langle \sigma w_0 \rangle / (m_i + m_n) = 9.21 \times 10^{13}$ , where we take  $\sigma = 10^{-15} \text{ cm}^2$ , and an effective velocity of  $w_0 = 1.9 \times 10^6 \text{ cm s}^{-1}$ . We quote our results in terms of the length, time, and

velocity scales given above, however, as this run will give results appropriate for  $A_n = 25$  shocks in a wide variety of conditions.

The resolution of our runs can best be expressed by giving the number of zones in the unperturbed shock thickness,  $L_{shk}$ . As shorthand, we use the format  $Lnn$ , where  $nn$  are the number of zones. We have performed runs with resolutions ranging from L60 to L240 (note that Stone [1997] used a standard resolution of L21, though he focussed on slower shocks that had longer wavelengths of maximum growth, as we discuss in § 5.1). For our two-dimensional cases we used grids ranging from  $160 \times 40$  to  $640 \times 160$  zones, while for the three-dimensional cases we used grids with  $160 \times 40 \times 40$  and  $267 \times 80 \times 40$  zones.

### 3. Numerical Methods

Mac Low et al. (1995) described the basic interface with the ZEUS code. Summarizing, that work made four approximations: isothermality of ions, electrons and neutrals, no electron-ion drift, ion density dependent in power-law fashion on neutral density, and no ion inertia or pressure. This allowed us to neglect, respectively, the energy equation, Ohmic diffusion, and the equations of ion mass and momentum conservation. This approach has proved adequate for modelling protostellar disks, but broke down for both physical and numerical reasons when applied to C-shocks. The Wardle instability depends on the flow of ions along buckling field lines in the shock front, and so was suppressed by the neglect of the ion mass conservation equation.

Neglect of ion inertia and pressure had allowed the replacement of the ion momentum conservation equation by an algebraic equation expressing the balance between Lorentz forces and ion-neutral drag in determining the drift velocity between ions and neutrals. This approach is physically accurate and allows time steps determined by the equivalent of the Courant condition for ambipolar diffusion,  $\Delta t \leq \pi \gamma \rho_i \rho_n (\Delta x)^2 / |\mathbf{B}|^2$  (Mac Low et al. 1995). However, both Tóth (1994) and we have found that this approach is numerically unstable in the presence of steep velocity gradients as in C-shocks. Tóth (1994) found that even an explicit treatment of the ion momentum equation was insufficient to entirely suppress numerical instability; Tóth (1995) showed that a semi-implicit treatment of this equation was far more stable, an approach we have followed with some modifications described below.

The equations we solve in the current version of the code are then the neutral and ion continuity equations, the induction equation, and the neutral and ion momentum equations:

$$\partial \rho_n / \partial t = -\nabla \cdot (\rho_n \mathbf{v}_n) \quad (1)$$

$$\partial \rho_i / \partial t = -\nabla \cdot (\rho_i \mathbf{v}_i) \quad (2)$$

$$\begin{aligned}\rho_n(\partial \mathbf{v}_n / \partial t) &= -\rho_n(\mathbf{v}_n \cdot \nabla) \mathbf{v}_n - \nabla P_n \\ &\quad + \gamma \rho_i \rho_n (\mathbf{v}_i - \mathbf{v}_n)\end{aligned}\tag{3}$$

$$\begin{aligned}\rho_i(\partial \mathbf{v}_i / \partial t) &= -\rho_i(\mathbf{v}_i \cdot \nabla) \mathbf{v}_i - \nabla P_i + \gamma \rho_i \rho_n (\mathbf{v}_n - \mathbf{v}_i) \\ &\quad + (1/4\pi)(\nabla \times \mathbf{B}) \times \mathbf{B}\end{aligned}\tag{4}$$

$$(\partial \mathbf{B} / \partial t) = \nabla \times (\mathbf{v}_i \times \mathbf{B})\tag{5}$$

$$\nabla \cdot \mathbf{B} = 0\tag{6}$$

where the subscripts  $i$  and  $n$  refer to the ions and neutrals,  $\rho$ ,  $\mathbf{v}$ , and  $P$  are density, velocity and pressure for each fluid,  $\mathbf{B}$  is the magnetic field, and  $\gamma$  is the collisional coupling constant between the ions and neutrals.

We treat the ions as a separate fluid in the code, using the standard ZEUS algorithms to update them, except in the momentum equation where we make several changes to implement the semi-implicit algorithm. The basic idea of this new algorithm is to treat the stiffest terms in the equation implicitly, but maintain the standard operator splitting for the other terms. Tóth (1995) included the drag term and the transported fluxes in his semi-implicit computation. We find that we also needed to include the magnetic pressure forces in order to maintain balance between them and the drag terms.

We rewrite equations (3) and (4) in conservative form using momenta  $\mathbf{s} = \rho \mathbf{v}$ , and momentum fluxes  $F_n$  and  $F_i$ , and place them in finite difference form. We then get two equations in the two unknowns  $\mathbf{s}_n^{n+1}$  and  $\mathbf{s}_i^{n+1}$  for our implicit system:

$$\frac{\mathbf{s}_n^{n+1} V^{n+1} - \mathbf{s}_n^n V^n}{\Delta t} = -\nabla F_n\tag{7}$$

$$\begin{aligned}&+ \gamma V^{n+1} (\rho_n \mathbf{s}_i^{n+1} - \rho_i \mathbf{s}_n^{n+1}), \\ \frac{\mathbf{s}_i^{n+1} V^{n+1} - \mathbf{s}_i^n V^n}{\Delta t} &= -\nabla \left( F_i + \frac{\mathbf{B}^2}{8\pi} \right) \\ &+ \gamma V^{n+1} (\rho_i \mathbf{s}_n^{n+1} - \rho_n \mathbf{s}_i^{n+1}),\end{aligned}\tag{8}$$

where time levels are given by superscripts, the finite difference time step is  $\Delta t$ , and the inclusion of zone volumes  $V$  allows for a moving grid. We find the semi-implicit update to the momenta by solving these equations for  $\mathbf{s}_n^{n+1}$  and  $\mathbf{s}_i^{n+1}$ :

$$\begin{aligned}\mathbf{s}_n^{n+1} &= \\ &\left\{ (\mathbf{s}_n^n V^n - \nabla F_n \Delta t) (1 + \gamma \Delta t \rho_n) \right. \\ &+ \left. \gamma \Delta t \rho_n (\mathbf{s}_i^n V^n - \nabla \left[ F_i + \frac{\mathbf{B}^2}{8\pi} \right] \Delta t) \right\} \\ &\{ [1 + \gamma \Delta t (\rho_n + \rho_i)] V^{n+1} \}^{-1},\end{aligned}\tag{9}$$

$$\begin{aligned} \mathbf{s}_i^{n+1} = & \left\{ (\mathbf{s}_i^n V^n - \nabla \left[ F_i + \frac{\mathbf{B}^2}{8\pi} \right] \Delta t) (1 + \gamma \Delta t \rho_i) \right. \\ & + \left. \gamma \Delta t \rho_i (\mathbf{s}_i^n V^n - \nabla F_n \Delta t) \right\} \\ & \{ [1 + \gamma \Delta t (\rho_n + \rho_i)] V^{n+1} \}^{-1}. \end{aligned} \tag{10}$$

Of course, the magnetic pressure updates must be removed from the source step where they would normally be performed.

Unfortunately, including the ion momentum equation limits our timestep to  $\Delta t \leq \Delta x / v_{Ai}$ , and we can no longer use the substepping scheme described by Mac Low et al. (1995). As a result, computations through a flow time require many  $\times 10^5$  cycles. The total number of cycles goes as  $\chi^{1/2}$ , however, so increasing the ionization fraction helps, so long as it does not get so high that no C-shock is possible. Tóth (1995) showed that a faster algorithm could be implemented by going to a fully implicit method, at the cost of greatly increased code complexity.

For initial conditions we used a numerical solution for an isothermal C-shock (Smith & Mac Low 1997) interpolated onto our grid. We then added a random zone-to-zone fluctuation to the neutral velocity. In order to maintain the shock stationary on our grid, we set up the grid with defined values for the field variables at both ends—that is with “inflow” boundaries, but with the right side having a negative inflow velocity. We used periodic boundaries along the sides of the grid.

We can maintain the steady-state C-shock indefinitely in one dimension (Smith & Mac Low 1997). In two and three dimensions, we can maintain it for many thousands of cycles until the physical instability sets in, as shown in Figure 2. We also showed that we converge on the steady-state solution starting from a discontinuous initial condition in Smith & Mac Low (1997).

## 4. Instability

### 4.0.1. Linear growth

Let us begin by verifying that we are indeed seeing the instability in the linear regime. We follow Stone (1997) in using the magnetic energy in the field component parallel to the shock velocity,  $B_x^2$ , as a diagnostic. The growth rate depends almost entirely on the neutral Alfvén number of the gas and the angle of the shock to the field, as discussed by Wardle

(1990) and Tóth (1994). The analytic growth rate  $s$  can be derived from Figure 7 of Wardle (1990). Note, however, that that Figure gives the quantity  $st_{flow}$ , and that it appears to assume the value of  $t_{flow}$  given in Wardle’s equation (2.12). The parameters quoted by Wardle would actually give a coefficient of 5.4 rather than 5.0, but that does not agree with our numerics, while 5.0 does. (Note that, for the parameters we use, the coefficient is 6.5, but that is due to our different choices of  $m_i$  and so forth.)

In Figure 3 we show the parallel field energy as a function of time for our standard case for numerical resolutions of L60, L120, and L240. For this case, we derive a value of  $s = 42.5t_{flow}^{-1}$ , using Wardle’s value of the coefficient. In Figure 3 we show curves corresponding to  $s = (41, 42.5, 44)t_{flow}^{-1}$ , showing the excellent agreement with the analytic value. We have also measured the growth rate for our  $A_n = 10$  run, and get equally good agreement with the analytic value of  $s = 4.2t_{flow}^{-1}$ .

#### 4.0.2. *Nonlinear Development*

The striking feature of the nonlinear development is the formation of long, thin filaments of dense gas. These filaments begin to merge with each other so that the wavelength of the instability grows as it becomes increasingly nonlinear. (The nonlinear Rayleigh-Taylor instability also develops merging filaments, as described by Read [1984] and Youngs [1984]). We show this development in Figure 4.

In our standard model, numerical instabilities prevent computation of the further development of the filaments after the last time shown in Figure 4. However, we have been able to extend our computations of lower neutral Alfvén number shocks to later times, as shown in Figure 5. We confirm the finding of Stone (1997) that, in the nonlinear stage when the distance between filaments reaches the shock thickness, a new filament appears between the existing ones.

The thickness of the region between the initial ion deceleration zone and the final post-shock region increases with time as shown in Figure 6. The thickness grows with a velocity just equal to the post-shock velocity of the shock. It appears that once the instability is established, it does not relax back to a uniform medium easily, if at all. The post-shock state is thus a tree of merging filaments (or in three dimensions, merging sheets, as we discuss below.)

We find that the filaments’ width drops to the single zone level at every resolution that we have run the problem. Stone (1997) suggests that gas pressure eventually limits their thickness, but points out that the resolution needed to see this effect would be enormous,



requiring a dynamic range over  $10^4$ . We have confirmed this empirically by running several different Mach 25 runs with sound speeds as high as  $0.4v_{An}$  at our highest resolution, with no discernible difference in their evolution. However, as we show next, the filaments are probably manifestations of the Brandenburg & Zweibel (1994, 1995; hereafter BZ) ambipolar diffusion singularity, which they showed in the simplest case overwhelms thermal pressure, and so may well become extraordinarily thin.

#### 4.1. Ambipolar Diffusion Singularity

In Figure 7 we show the components of the magnetic field parallel and perpendicular to the shock velocity, along with the magnetic pressure. Although the perpendicular component remains dominant, as can be seen in the magnetic pressure plot, the parallel component undergoes a sharp reversal at each filament. A profile of the parallel field is shown in Figure 8. The field lines thus are basically perpendicular, but with extremely sharp kinks in them at each filament. The reversal in the parallel component appears to be enough to drive the BZ ambipolar diffusion singularity. This singularity steepens magnetic pressure gradients in the presence of ambipolar diffusion, due to the nonlinear nature of the ambipolar diffusion.

The actual field behavior that we compute can be understood analytically. The simulations demonstrate that the magnetic field parallel to the flow,  $B_x$ , grows exponentially (Fig. 3), evolving towards a saw-tooth structure as the filaments become thinner. That is,  $B_x$  becomes a linear function of  $y$ . In contrast, the ambipolar diffusion analysis of Brandenburg and Zweibel (1994) delivers a relation  $B_x \propto y^{1/3}$ . Their analysis, however, assumed the magnetic field to be zero within the filament whereas here we have the opposite case: the field  $B_y$  dominates. Hence to understand these different relationships we undertake a more general analysis.

The aim, following BZ, is to search for hydrostatic steady flow solutions to the induction equation. To begin we take the streaming (or drift) velocity from equation (4)

$$\mathbf{v}_D = (\mathbf{v}_n - \mathbf{v}_i) = -(1/4\pi\gamma\rho_i\rho_n)(\nabla \times \mathbf{B}) \times \mathbf{B} \quad (11)$$

to eliminate the ion velocity from the induction equation (5):

$$(\partial\mathbf{B}/\partial t) = \nabla \times (\mathbf{v}_n \times \mathbf{B}) + (1/4\pi\gamma\rho_i\rho_n)\nabla \times [\{(\nabla \times \mathbf{B}) \times \mathbf{B}\} \times \mathbf{B}]. \quad (12)$$

We take a uniform flow in the x-direction i.e.  $B_x(y)$ ,  $v_{xn}(y)$  and  $B_y = B_0$ , a constant as required for vanishing divergence. Ignoring field amplification due to the first shear term

(that is, taking  $v_{xn}$  constant), the induction equation becomes

$$4\pi\gamma\rho_i\rho_n\frac{dB_x}{dt} = (B_0^2 + B_x^2)\frac{d^2B_x}{dy^2} + 2B_x\left(\frac{dB_x}{dy}\right)^2. \quad (13)$$

The solution to the steady state form is

$$y = k_1 + k_2 \left[ 2 \tan \theta + \frac{\tan^3 \theta}{\sin^2 \theta} \right] \quad (14)$$

where the field angle  $\theta = \arctan(B_x/B_0)$ , and  $k_1$  and  $k_2$  are integration constants. The second term dominates and yields the Brandenburg & Zweibel (1994) solution in the limit  $B_0 \rightarrow 0$ . Such a solution may be relevant to the study of parallel-field C-shocks that we plan. The first term, however, dominates for the case studied here, and indeed predicts a linear  $y - B_x$  behaviour.

This singularity steepens magnetic pressure gradients in the presence of ambipolar diffusion, due to the nonlinear nature of the ambipolar diffusion. Among other things, the resulting steep gradients trigger numerical instabilities, visible as the single-zone regions of opposed field along the filaments. These regions produce anomalous fields and extremely high ion velocities, reducing the timestep to impractically small values. Physically, the exceedingly sharp discontinuities in field direction produced by this singularity will drive strong current sheets along the filaments, with uncertain consequences probably including heating and possibly the production of energetic particles.

## 4.2. Three-Dimensional Structure

To study the three-dimensional structure of the instability we performed two runs at L120. One was of our standard case, while the other had a zone-to-zone perturbation  $\delta v_{n1}/v_{n1} = 10^{-6}$  rather than 0.01. We found that the thin filaments seen in the two-dimensional models developed in the low perturbation run into coherent mildly rippled layers, as shown in Figure 9. In the standard case, on the other hand, we found that each vertical plane developed essentially independently, resulting in spikes rather than layers. This appears to have been an effect of the initial perturbation, suggesting that the structure in the third dimension in nature will be determined by the existing perturbation structure in the pre-shock gas unless it is quite uniform on scales of  $L_{shk}$ .

### 4.3. Resolution Studies

In order to understand the effects of numerical diffusivity on our results, we ran our standard case in two dimensions at resolutions of L60, L120, and L240, and in three dimensions at resolutions of L60 and L120, as we discussed at the beginning of this section. We show the density distribution at the end of the run for these three different cases in two dimensions in Figure 10. Examining this figure, it is clear that the filamentary nature of the nonlinear instability has been well resolved, but that we have not converged on the exact value of the wavelength of maximum growth. As was shown in Figure 6, the thickness of the shocked layer is converged to within a few percent.

The thickness of individual filaments in the transverse direction appears to be determined entirely by the dissipation scale physically, due to the BZ ambipolar diffusion singularity, as we discussed above, in § 4.0.2 Effectively, they become infinitely thin. Indeed, they reach thicknesses of one or two zones at every resolution, at which point the extreme gradients cause numerical instabilities.

## 5. Variations on the Theme

### 5.1. Mach Number Dependence

In the linear regime, the growth rate and wavelength of maximum growth depend on the neutral Alfvén number,  $A_n$ , as shown by Wardle (1990), and confirmed in some detail by Tóth (1994, 1995), as well as in Figure 3. The slower growth rate and longer wavelength of maximum growth in the shock with  $A_n = 10$  shown in Figure 5, as compared with our standard model, agree with the linear theory. We find qualitative differences in the nonlinear development of the instability at different  $A_n$  as well, as can be seen by comparing Figures 4 and 5. At lower values of  $A_n$ , the larger wavelength of maximum growth means that there is more space between the resulting filaments, and each one is thicker compared to the initial shock thickness.

### 5.2. Ionization Equilibrium

Until now, we have assumed that ionization and recombination timescales were long compared to the flow time through the shock  $t_{flow}$ . If both ionization and recombination timescales are very short compared to the flow time, the ion density will remain constant with time, or vary as a power law of the neutral density, suppressing the instability. The

version of ZEUS described by Mac Low et al. (1995) works in this regime, so we ran our standard case with constant ion density using that version. We did indeed find that after  $0.4t_{flow}$  there was no indication of the Wardle instability. At that point, however, the run was ended by numerical instabilities caused by the large ion-neutral streaming velocities, which caused strong zone-to-zone fluctuations in the computed parallel velocities. In Figure 11 we compare the neutral density distribution for our standard initial conditions to the result for constant ion density, to show the lack of evolution.

### 5.3. Initial Perturbations

The form and strength of the initial perturbations we use to trigger the instability can make a difference in the results. In our first runs we used a 1% zone-to-zone perturbation in density; later we followed Tóth (1995) in using perturbations in parallel neutral velocity  $v_{n1}$  instead, with magnitudes of 1% and 0.0001%. We found that 1% perturbations were already large enough to significantly change the final nonlinear results, especially in three dimensions, as we discussed in § 4.2. Even in two dimensions, the larger perturbations change the wavelength of maximum growth significantly, as shown in Figure 12, where the nonlinear development of the standard case is compared to that of a low perturbation case, which develops a longer wavelength.

## 6. Implications for Molecular Hydrogen Emission

One measurable consequence of the C-shock instability is that the line emission directly from the shocked layer will differ from the steady-state case, and should even be a slowly varying function of time. Warm C-shocks vibrationally excite the hydrogen molecules. We may thus expect that the fraction of  $H_2$  in higher vibrational levels would decrease with time as frictional heating is spread out over a thicker layer. To test this, we employ the “cool C-shock” approximation, that requires the temperature  $T \ll 2m_H v_s^2/k$ . This is valid provided cooling is very efficient so that the thermal pressure and pressure gradient can be neglected. Then, the isothermal assumption is not critical to the flow pattern so long as a low temperature is chosen. In this case, an effective temperature can be derived at each location by equating the frictional heating to the molecular and atomic cooling (see Smith & Brand 1990a, Smith 1993).

The cooling functions we use here have the form  $n_n^{1+f} T^\alpha \text{ erg s}^{-1} \text{ cm}^{-3}$ . We study two cases: the high-density regime with  $\rho_n \sim 10^8 \text{ cm}^{-3}$ , where  $H_2O$  cooling dominates,

$f = 1$ , and  $\alpha = 1.2$ ; and the low density regime with  $\rho_n \sim 10^{4-6} \text{ cm}^{-2}$ , where  $\text{H}_2$  cooling dominates,  $f = 0$ , and  $\alpha = 3.3$  (Smith 1993). Frictional heating is  $\propto n_n n_i v_{in}^2$ . This yields  $T^\alpha = \eta v_{in}^2 n_i / n_n^f$ , where we choose the constant  $\eta$  so that the initial C-shock possesses a maximum temperature of 2,500 K. The temperature distribution for the two different cooling cases is shown in Figure 13 for the initial state and a time  $0.36 t_{flow}$ , after the instability has gone nonlinear.

The column density of  $\text{H}_2$  molecules in an excited state  $j$  with energy level  $kT_j$  is given by

$$N_j = \frac{1}{4} g_j N(\text{H}_2) \exp(-T_j/T) / Z(T). \quad (15)$$

The statistical weights  $g_j = 4\psi(2J_j + 1)$ , where  $\psi$  is the fraction of  $\text{H}_2$  molecules in the ortho state (assumed to be 0.75 here),  $J_j$  is the rotational quantum number, and  $Z(T)$  is the partition function

$$Z(T) = 6.13510^{-3} T [1 - \exp(-5850/T)]^{-1}, \quad (16)$$

(Smith, Davis & Lioure 1997), assuming local thermodynamic equilibrium. The intensity of a line is then given by

$$L_j = (hc/\lambda_j) N_j A_j, \quad (17)$$

where the radiative deexcitation rates  $A_j$  (Turner, Kirby-Docken, & Dalgarno 1977), along with statistical weights, wavelengths (Black & Dishoeck 1987), and excitation temperatures for a number of important lines are given in Table 1.

Neufeld & Stone (1997) concluded that the Wardle instability would not markedly change the emission expected from steady-state C-shocks. However, they only considered shocks with neutral Alfvén number  $A_n = 10$  and  $n_0 = 10^5 \text{ cm}^{-3}$ , which will be dominated by molecular hydrogen cooling. While we agree that the emission from these shocks is not strongly modified by the Wardle instability, we now show that shocks in other regions of parameter space behave much differently.

One common method of deducing molecular excitation is examining the ratio of the strong  $\text{H}_2$  lines 1-0 S(1) and 2-1 S(1), which should increase as a gas cools and the second vibrational level becomes less populated. We calculate the column density of molecules in each grid zone, and then sum over zones to find the total number of molecules on the grid in each upper energy level,  $N_j$ . Radiative transfer could be added in this treatment. However these quadrupole transitions are expected to be optically thin. Figure 14 shows the ratio of line intensities  $L(1-0 \text{ S}(1))/L(2-1 \text{ S}(1))$ , ignoring foreground extinction, as a function of time and numerical resolution for both our standard case and our model with  $A_n = 10$ . We find that the instability can shift the ratio strongly when  $\text{H}_2\text{O}$  cooling dominates at  $A_n = 25$ ,

and more weakly in other cases. We have not converged on the actual value of the shift at our current numerical resolution, primarily because the hot filaments seen in Figure 13 are not yet well resolved. As unimportant physics is probably also important there, higher resolution runs are not particularly justified.

A more general method of determining the molecular excitation is to correlate column densities (which can be derived from line intensities using equation 17 and Table 1) in a number of lines against the excitation temperatures of the lines. Because of the strong temperature dependence of the column densities in equation 15, we scale the column densities by  $g_j \exp(-T_j/2000K)$ , the temperature dependence of a slab of gas with temperature 2000 K, where the statistical weights  $g_j$  and excitation temperatures  $T_j$  for important lines are given in Table 1. In Figure 15, we show the resulting time-dependent development of the excitation conditions for our standard case with either H<sub>2</sub>O and H<sub>2</sub> cooling dominant. The instability forms both hot and cold regions compared to the steady-state C-shock, and so produces a marked shift in the integrated excitation conditions across the shock.

Finally we can examine the detailed line profiles produced by stable and unstable C-shocks. We compute them by binning the grid into angle-dependent velocity bins, and then adding up the intensity of emission from all zones in each bin (scaled by the square of the zone-size for runs of different linear resolution) to get a spectrum. We smooth the resulting profiles with a 1 km s<sup>-1</sup> Gaussian (except for the narrow profile from a line of sight perpendicular to the shock velocity, which we smooth with an 0.1 km s<sup>-1</sup> Gaussian). The intensity scales displayed are arbitrary, but consistent across all plots to allow comparison between lines and angles.

We first examine the effects of angle and numerical resolution on profiles of the bright 1-0 S(1) line in Figure 16. We show the line profile for lines of sight parallel to the shock velocity, at 45° to it, and perpendicular to it, for shocks dominated by H<sub>2</sub>O and H<sub>2</sub> cooling. Note that the velocity scale is different for each angle in the figure. We find that the line is broadened to the Alfvén velocity even on lines of sight normal to the shock velocity. We find that the details of our profiles are dependent on our numerical resolution, as can be seen by comparing different line profiles in each plot, which are from runs differing by a factor of two in linear resolution. However, the gross shape and intensity of each line appears well described. The smaller scale variation is due to the dependence of the results on the details of the filament structure where most of the hot gas is produced. Again, the structure of these filaments is also liable to be influenced by physics not yet included in our model.

Finally, we examine the profiles of a number of lines observable with ISO (Figure 17), in the K-band, or with NICMOS on the *Hubble Space Telescope* (Figure 18), for cooling

dominated either by  $\text{H}_2$  or by  $\text{H}_2\text{O}$ . We show in grey the profiles predicted for a steady-state C-shock viewed parallel to the shock velocity. These are very well resolved, and represent the first publication of predicted line profiles for most of these lines; they agree well with the general predictions of Smith & Brand (1990b). In black we show the same profiles at the end of our standard run, showing the shifts in line profile and intensity due to the growth of hot and cold regions due to the instability. We also give the derived total column densities from these lines in Table 1 to allow computation of arbitrary line ratios. The convergence of the unstable profiles can be judged by comparison with Figure 16. The general direction and size of the shift from the steady-state value is probably correct, but the quantitative results are probably good to no better than 20%. The general trend we observe is a strengthening of lines at the soft and hard ends of the spectrum due to the broader range of temperatures in the C-shock, as well as changes in the velocity structure due to the filaments.

## 7. Summary

- The fastest growing modes of the Wardle (1990) C-shock instability are layers with thickness of order  $0.1L_{shk}$  in the plane parallel to the field and the shock normal, in agreement with Wardle’s linear analysis. As predicted, our standard shock with neutral Alfvén number  $A_n = 25$  goes unstable quite rapidly, becoming very non-linear in a fraction of  $t_{flow}$ .
- When the shock goes non-linear, the layers collapse into thin, dense filaments (sheets in three dimensions) with density more than a factor of two above the expected post-shock density. A dense sheet also forms across the shock front at the downstream end of the filaments. These filaments are physically probably too thin to be well-resolved numerically. Tóth (1994, 1995) did not see these filaments, possibly due to the diffusivity of his code, but Stone (1997) finds a similar morphology.
- As the instability becomes more nonlinear, the sheets collapse toward each other, as seen in the upper panels of Figure 4. Thus, longer wavelength modes become dominant as time goes on. This process has proceeded in some of our runs until only one wavelength is left on the grid. Rayleigh-Taylor instabilities undergo a similar lengthening of the dominant mode in the non-linear regime. New filaments appear when the distance between filaments becomes comparable to shock thickness.
- The thickness of the shock front increases linearly as the filaments grow, with the ion velocity dropping sharply at the ends of the growing filaments.

- The Brandenburg & Zweibel (1994, 1995) ambipolar diffusion singularity steepens the fields along the filaments, forcing the filaments to be ever thinner, until the code breaks down due to the resulting sharp gradients. Strong current sheets form along the filaments as a result, with consequences that probably include heating and ionization, and possibly the production of energetic particles. The physics of these filaments have not been completely captured with our approximations.
- We compare the integrated excitation conditions across stable and unstable C-shocks, giving comparisons of scaled column density to line excitation temperature, line profiles, and line ratios for our standard case. These results are sensitive to the as yet unmodeled physics of the filaments, as well as numerical resolution of the very thin filaments, but probably give a generally correct description of the effect of the instability on observables from C-shocks.
- Significant variations in emission line properties are predicted on timescales of fractions of  $t_{flow} = (30/n_i)$  yr, where  $n_i$  is the ion number density. Thus, multiple observations of suspected C-shocks in dense regions should prove rewarding.

We thank J. Stone for generously sharing his results prior to submission, S. Beckwith for emphasizing the need for predictions of multiple line properties, and E. Zweibel for discussions of the ambipolar diffusion singularity. MDS thanks the DFG for financial support. Computations were performed at the MPG Rechenzentrum Garching.



## REFERENCES

- Black, J. H. & Dishoeck, E. F. 1987, *ApJ*, 322, 412
- Black, D. C., & Scott, E. H. 1982, *ApJ*, 263, 696
- Brandenburg & Zweibel, 1994, *ApJ*, 427, L91
- Brandenburg & Zweibel, 1995, *ApJ*, 448, 734
- Draine, B. T. 1980, *ApJ*, 241, 1021
- Draine, B. T., & McKee, C. F. 1993, *ARA&A*, 31, 373
- Fiedler, R. A., & Mouschovias, T. Ch. 1992, *ApJ*, 391, 199
- Königl, A. 1989, *ApJ*, 342, 208
- Mac Low, M.-M., Norman, M. L., Königl, A., & Wardle, M. 1995, *ApJ*, 442, 726
- Mac Low, M.-M. & Smith, M. D. 1997, in *Low Mass Star Formation—from Infall to Outflow; Poster Proceedings of the IAU Symposium No. 182*, eds. F. Malbet and A. Castets (Grenoble, France: Obs. de Grenoble), p. 155
- Mestel, L. & Spitzer, L. Jr. 1956, *MNRAS*, 116, 504
- Mouschovias, T. Ch. 1979, *ApJ*, 228, 475
- Mouschovias, T. Ch., & Morton, S. A. 1991, *ApJ*, 371, 296
- Neufeld, D. A. Stone, J. M. 1997, *ApJ*, submitted
- Paleologou, E. V., & Mouschovias, T. Ch. 1983, *ApJ*, 275, 838
- Read, K. I. 1984, *Physica*, 12D, 45
- Smith, M. D. 1993, *ApJ*, 406, 520
- Smith, M. D. & Brand, P. W. J. L. 1990a, *MNRAS*, 242, 495
- Smith, M. D. & Brand, P. W. J. L. 1990b, *MNRAS*, 243, 498
- Smith, M. D., Davis, C. J., & Lioure, A. 1997, *A&A*, submitted
- Smith, M. D. & Mac Low, M.-M. 1997, *A&A*, submitted
- Stone, J. M. 1997, *ApJ*, submitted
- Neufeld, D. A. & Stone, J. M. 1997, *ApJ*, submitted
- Stone, J. M., & Norman, M. L. 1992a, *ApJS*, 80, 753
- . 1992b, *ApJS*, 80, 791
- Tóth, G. 1994, *ApJ*, 425, 171

- Tóth, G. 1995, MNRAS, 274, 1002
- Turner, J., Kirby-Docken, K. & Dalgarno, A. 1977, ApJS, 35, 281
- Youngs, D. L., 1984. Physica, 12D, 32
- Wardle, M. 1990, MNRAS, 246, 98
- . 1991, MNRAS, 250, 523
- . 1991, MNRAS, 251, 119

Table 1. Representative Molecular Hydrogen Lines

Line	$\lambda^a$	$T_j^b$	$A_j^c$	$g_j^d$	H <sub>2</sub> O cooling <sup>e</sup>		H <sub>2</sub> cooling	
					$t = 0$	$0.36t_{flow}$	$t = 0$	$0.36t_{flow}$
2-0 S(5)	1.0848	15763.	3.28	45.	3.1e1	2.4e1	1.5e1	2.9e1
1-0 S(3)	1.9570	8365.	4.21	33.	6.3e2	3.9e2	3.1e2	1.9e2
2-1 S(4)	2.0035	14764.	5.57	13.	1.4e1	9.9e0	6.9e0	1.1e1
1-0 S(2)	2.0332	7584.	3.98	9.	2.5e2	1.6e2	1.2e2	7.1e1
2-1 S(3)	2.0729	13890.	5.77	33.	5.2e1	3.5e1	2.6e1	3.3e1
1-0 S(1)	2.1213	6951.	3.47	21.	7.9e2	5.0e2	3.9e2	2.2e2
2-1 S(2)	2.1536	13150.	5.60	9.	2.0e1	1.3e1	9.7e0	1.1e1
3-2 S(3)	2.2008	19086.	5.63	33.	5.5e0	5.3e0	2.7e0	1.1e1
1-0 S(0)	2.2226	6471.	2.53	5.	2.4e2	1.5e2	1.2e2	6.5e1
2-1 S(1)	2.2471	12550.	4.98	21.	6.0e1	3.8e1	3.0e1	3.0e1
4-3 S(3)	2.3439	23956.	4.58	33.	6.9e-1	1.1e0	3.3e-1	5.1e0
3-2 S(1)	2.3858	17818.	5.14	21.	6.0e0	5.2e0	2.9e0	8.9e0

Table 1—Continued

Line	$\lambda^a$	$T_j^b$	$A_j^c$	$g_j^d$	H <sub>2</sub> O cooling <sup>e</sup>		H <sub>2</sub> cooling	
					$t = 0$	$0.36t_{flow}$	$t = 0$	$0.36t_{flow}$
0-0 S(9)	4.6950	10265.	4.90	69.	5.5e2	3.4e2	2.7e2	2.0e2
0-0 S(8)	5.0530	8682.	3.24	21.	3.5e2	2.1e2	1.7e2	1.1e2
0-0 S(7)	5.5110	7199.	2.00	57.	1.9e3	1.2e3	9.4e2	5.3e2
0-0 S(6)	6.1090	5833.	1.14	17.	1.1e3	7.4e2	5.4e2	3.0e2
0-0 S(5)	6.9100	4587.	0.588	45.	5.5e3	4.1e3	2.7e3	1.5e3
0-0 S(4)	8.0250	3476.	0.264	13.	2.9e3	2.4e3	1.4e3	8.3e2
0-0 S(3)	9.6650	2504.	0.0984	33.	1.4e4	1.3e4	6.5e3	4.1e3
0-0 S(2)	12.2790	1682.	0.0276	9.	6.6e3	7.6e3	3.1e3	2.3e3
0-0 S(1)	17.0350	1015.	0.00476	21.	2.9e4	4.1e4	1.3e4	1.2e4

<sup>a</sup>Wavelength in  $\mu\text{m}$

<sup>b</sup>Excitation temperature in K

<sup>c</sup>Einstein A-values for radiative deexcitation in  $10^{-7} \text{ s}^{-1}$

<sup>d</sup>Statistical weights

<sup>e</sup>Relative column densities for given times and cooling, where 1e4=  $1 \times 10^4$

Fig. 1.— The Wardle instability occurs when field lines are perturbed slightly. The neutral drag forces ions into the valleys, increasing the drag in the valleys and reducing it at the peaks. As a result, the valleys are further deepened, while magnetic pressure expands the peaks as well, driving an exponential instability.

Fig. 2.— Ion (earlier drop) and neutral (later drop) velocities scaled to the shock velocity. Dotted lines show the analytic solution, while solid lines show the two-dimensional higher resolution (grey) and three-dimensional (black) solutions after  $0.11t_{\text{flow}}$ . The three-dimensional solution has been shifted by  $1.5L_{shk}$  for visibility.

Fig. 3.— Growth of instability, as indicated by the growth of magnetic energy in the field component parallel to the shock velocity,  $B_x^2$ , normalized to the initial magnetic energy on the grid  $B_{y0}^2$ . Our standard case in two dimensions with neutral Alfvén number  $A_n = 25$  is shown at resolutions of L60 (dotted line), L120 (dashed line), and L240 (thick solid line). Overlaid are three exponentials (thin solid lines) of form  $e^{st}$ , with  $s = (41, 42.5, 44)t_{\text{flow}}^{-1}$ , where the analytic value is  $s = 42.5t_{\text{flow}}^{-1}$ , as discussed in the text. In three dimensions we show a run with the same parameters at a resolution of L120 and with smaller initial perturbations (thick solid line). The overlaid exponential (thin solid line) in this case is the analytic value of the growth rate, normalized appropriately.

Fig. 4.— Time history of (a) neutral parallel velocity, (b) neutral density, and (c) ion density for our standard model with a neutral Alfvén number  $A_n = 25$ , and other parameters given in the text, run at a resolution of L240 on a grid of  $640 \times 160$  zones.

Fig. 5.— Time history of ion density for our model with neutral Alfvén number  $A_n = 10$ , run at a resolution of L120 on a large grid of  $400 \times 240$  zones. The first indications of a density enhancement where another filament will form can be seen in the last panel, between the upper two filaments.

Fig. 6.— Shock thickness as a function of time at numerical resolutions of L60 (dotted), L120 (dashed), and L240 (solid), showing the near-linear growth in the size of the disturbed shocked region.

Fig. 7.— Parallel and perpendicular components of the field at the end of our standard run. Note that the field remains dominated by the perpendicular component.

Fig. 8.— Profile across filaments of the parallel field component  $B_x$  at the end of our standard run, at the midpoint of the grid in the  $x$ -direction. Values in individual grid zones are shown by triangles. Note the linear increase in the field, and the extremely sharp transitions in the filaments.

Fig. 9.— (a) Comparison of neutral  $x$ -velocity distribution in the  $x - y$  plane for two- and three-dimensional versions of the standard model at a resolution of  $L_{shk} = 120$  zones (total grid  $267 \times 80 \times 40$  zones). (b) Cuts through the  $y - z$  plane of the three-dimensional model at locations indicated by black lines in (a), scaled to the same palette.

Fig. 10.— Comparison of results for runs with resolutions of L60, L120, and L240. The log of the neutral density distribution is shown for three runs with total grids of  $160 \times 40$  zones,  $320 \times 80$  zones, and  $640 \times 160$  zones, for our standard model. Note the convergence of the morphology and the wavelength of maximum growth, as well as the consistent increasing trend in the peak density, which has not yet converged.

Fig. 11.— Comparison of runs with conserved ions versus constant ion density, showing that if ionization and recombination occur fast enough to maintain a constant ion density, the instability is suppressed. Log of neutral density is shown, with the same scaling across both images. The run with conserved ions is our standard model at a resolution of  $L_{shk} = 120$  zones, while the run with constant ion density was run with ion fraction  $\chi = 10^{-6}$  for speed. (This should make no physical difference, aside from changing the absolute time and length scales.) The run at constant ion density had to be halted due to numerical instability at this time, but no sign of physical instability was seen.

Fig. 12.— Density distribution for runs with the given initial perturbation strength (in both cases, perturbations consisted of zone-to-zone random changes in the parallel neutral velocity). The strong perturbation case is shown at a time  $t = 0.36t_{flow}$ , while the weak perturbation case is shown at a time  $t = 0.69t_{flow}$ . The strong perturbation standard case was only run with half the number of zones in the  $y$ -direction, so it has been doubled for comparison to the  $640 \times 320$  zone weak perturbation case.

Fig. 13.— When drag heating balances radiative cooling, the equilibrium temperature can be computed assuming that either (a) water or (b) molecular hydrogen dominates the cooling. We show the log of temperature for our standard model before the instability sets in, and after it has become nonlinear at a time  $0.36t_{flow}$ . The earlier time shows the standard picture of C-shocks, while the later time emphasizes the difference the instability makes. Note the existence of warm gas at the temperatures predicted by the standard picture, but mixed with colder and hotter gas.

Fig. 14.— Ratio of emission intensity from the 1–0 S(1) and 2–1 S(1) lines of molecular hydrogen for cooling dominated by (a) water and (b) molecular hydrogen for our  $A_n = 25$  run. Lighter grey lines show a numerical resolution of L60, darker grey lines are L120, and black lines are L240. (c) The same ratio is shown for our  $A_n = 10$  run for both molecular hydrogen cooling (dashed) and water cooling (solid).

Fig. 15.— Variation of excitation conditions in an unstable C-shock at times of 0 (lightest grey),  $0.19t_{flow}$ ,  $0.29t_{flow}$ , and  $0.36t_{flow}$  (black) for cooling dominated by (a) water and (b) molecular hydrogen. The column density is scaled by  $g_j \exp(-T_j/2000 \text{ K})$ , the functional form of column densities from a uniform slab of gas at a temperature of 2000 K, where the statistical weights  $g_j$  and excitation temperatures  $T_j$  are given in Table 1 for many common lines. Thus, such a uniform slab of gas would produce a flat line in this plot.

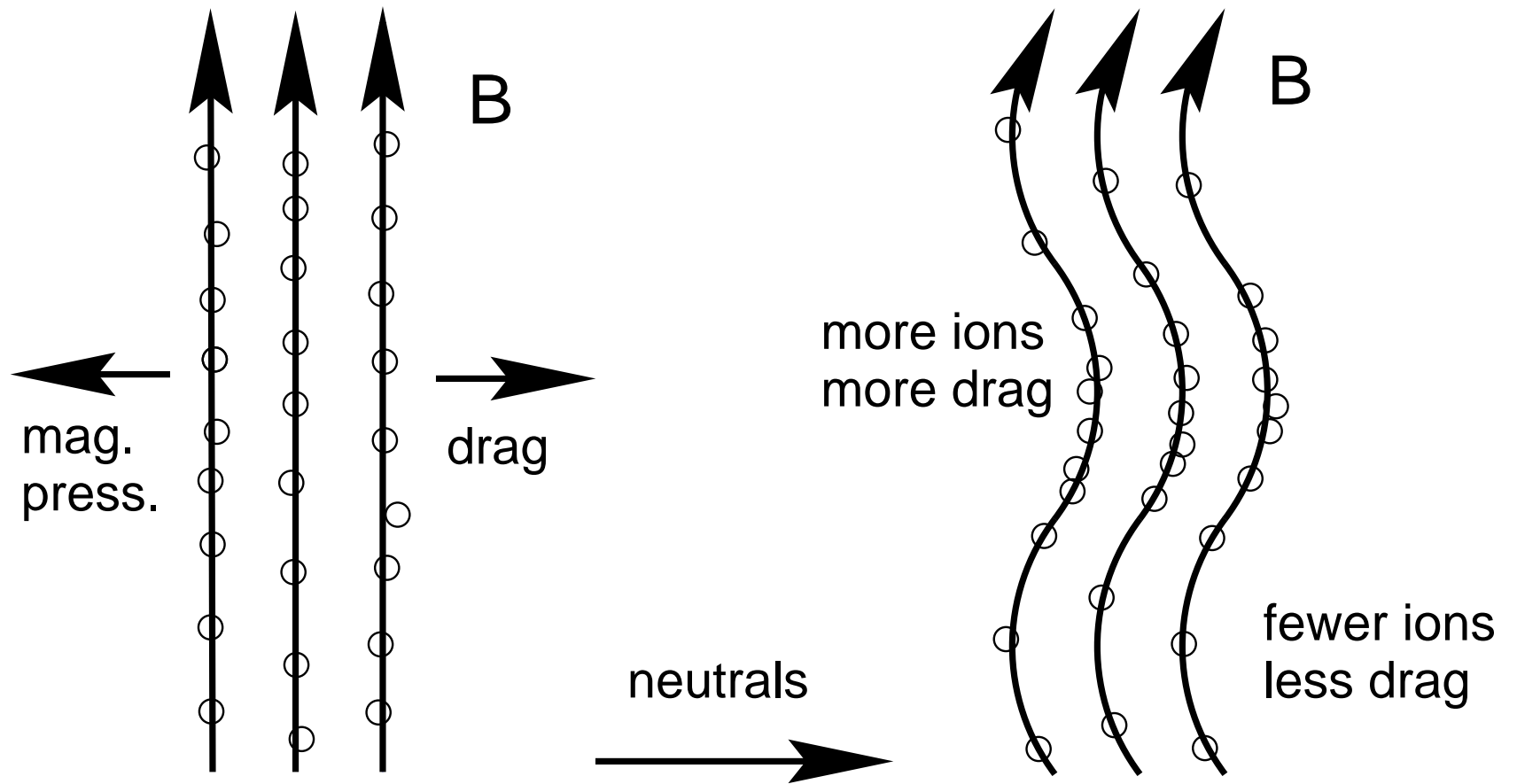
Fig. 16.— Variation with angle to the shock velocity of the line profile from the 1–0 S(1) line of  $\text{H}_2$  at  $2.121 \mu\text{m}$  in the final state of our standard case at resolutions of L60 (lighter grey), L120 (darker grey), and L240 (black), demonstrating the degree of numerical convergence expected for cooling dominated by (a) water and (b) molecular hydrogen. Note that the velocity axes are scaled by different values at each angle, with  $v_s = 25v_{A_n}$  for this shock with  $A_n = 25$ .

Fig. 17.— A comparison of line profiles from an unstable C-shock (black) to profiles from a steady-state C-shock with our standard initial parameters (grey) for a sample of  $\text{H}_2$  lines observable by ISO, assuming (a) water cooling and (b) molecular hydrogen cooling. The unstable C-shock profiles are computed from the final state of our highest resolution L240 run.

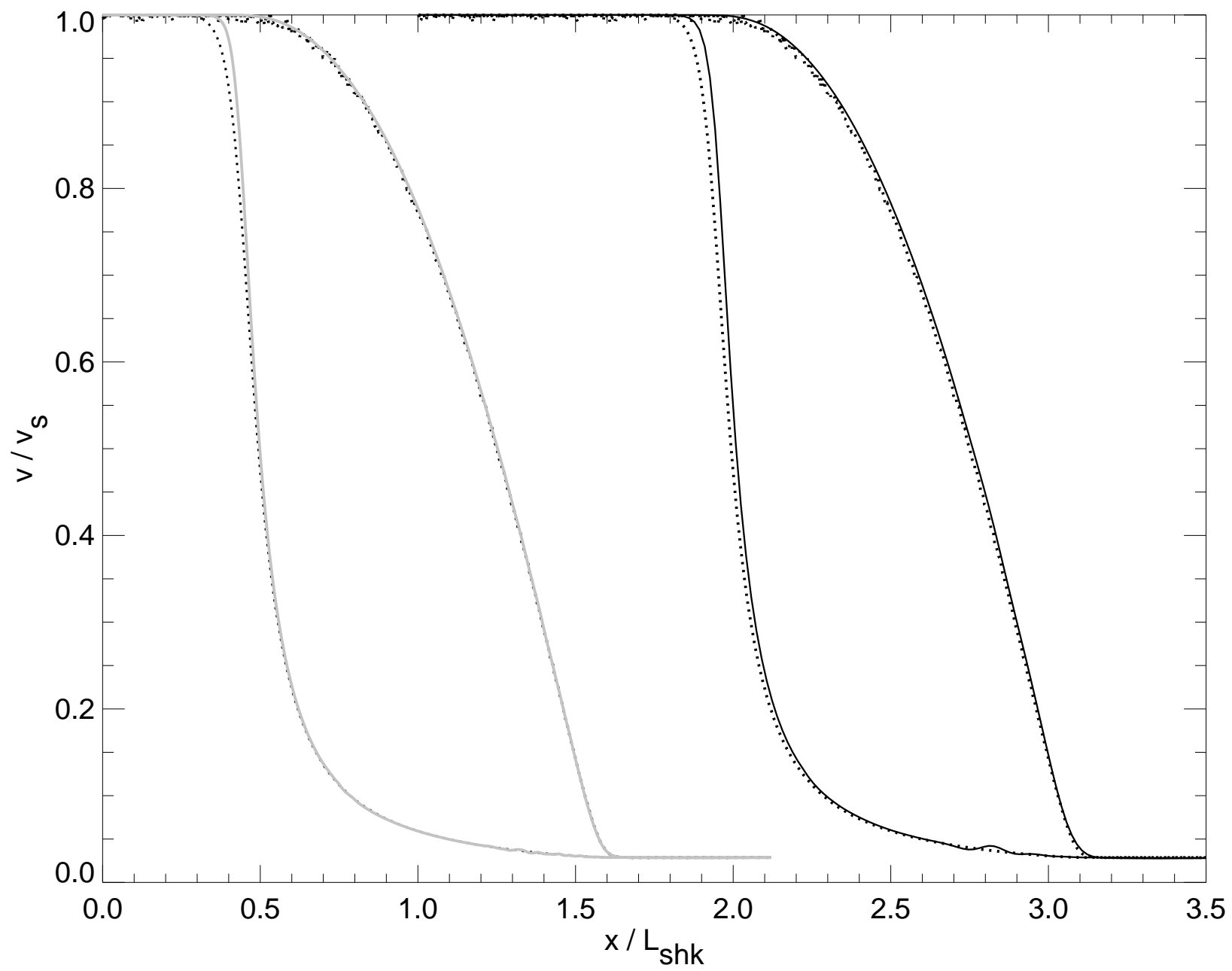
Fig. 18.— A comparison of line profiles from an unstable C-shock (black) to profiles from a steady-state C-shock with our standard initial parameters (grey) for a sample of near-IR  $\text{H}_2$  lines observable in the K-band, or with NICMOS on the HST, assuming (a) water cooling and (b) molecular hydrogen cooling. The unstable C-shock profiles are computed from the final state of our highest resolution L240 run.

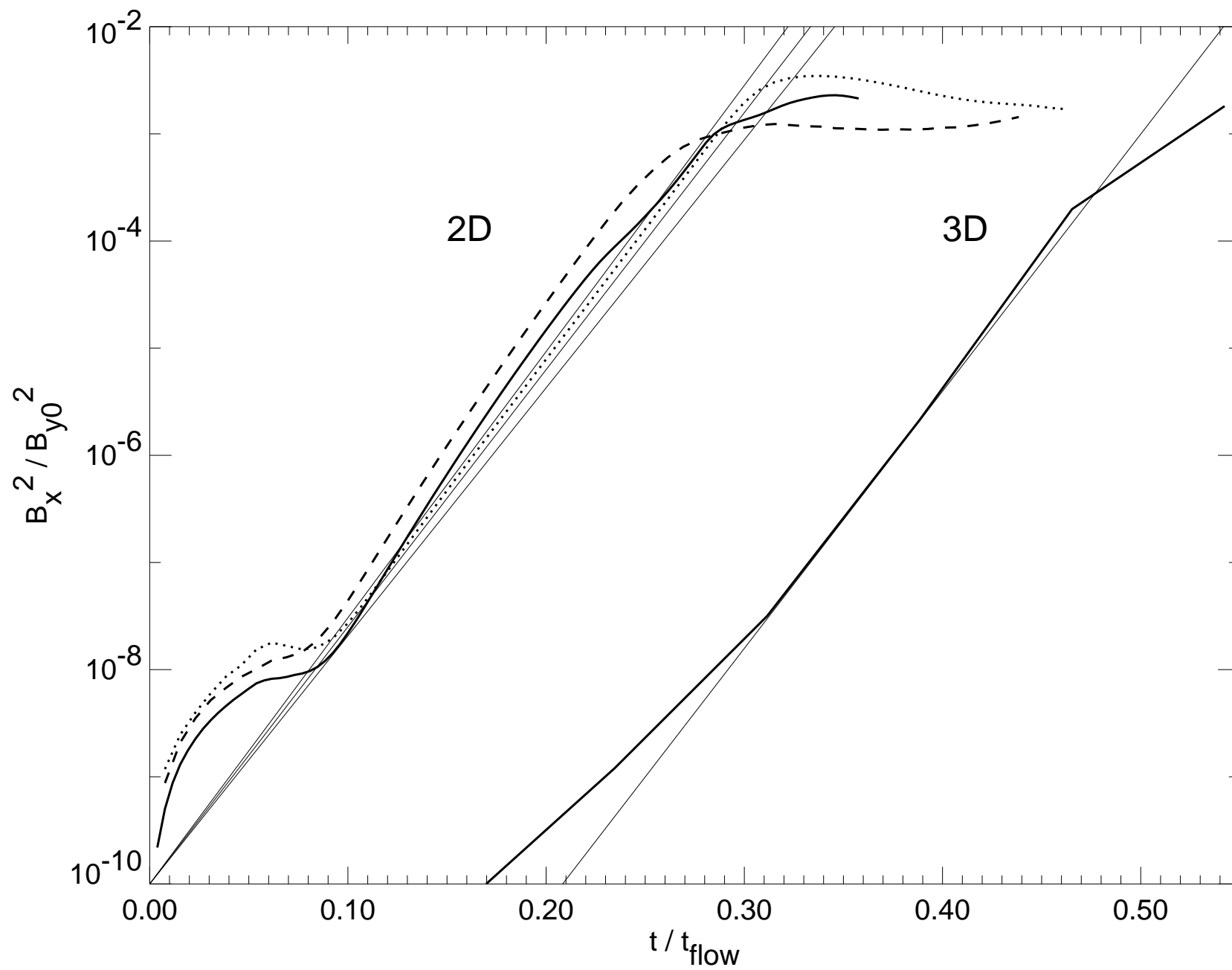


# Wardle Instability



(after Wardle 1990)





This figure "fig4a.jpg" is available in "jpg" format from:

<http://arxiv.org/ps/astro-ph/9703172v1>

This figure "fig4b.jpg" is available in "jpg" format from:

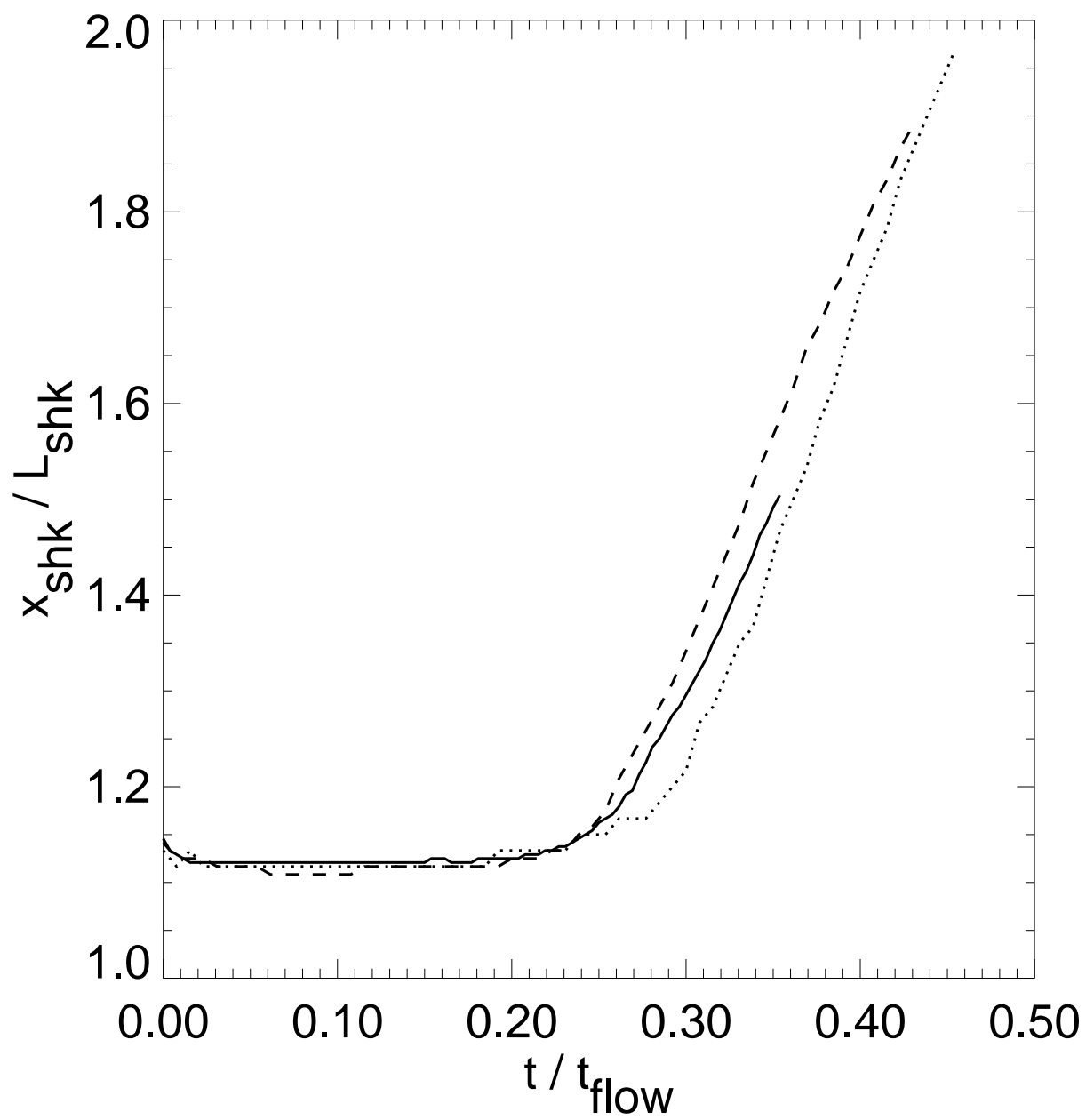
<http://arxiv.org/ps/astro-ph/9703172v1>

This figure "fig4c.jpg" is available in "jpg" format from:

<http://arxiv.org/ps/astro-ph/9703172v1>

This figure "fig5.jpg" is available in "jpg" format from:

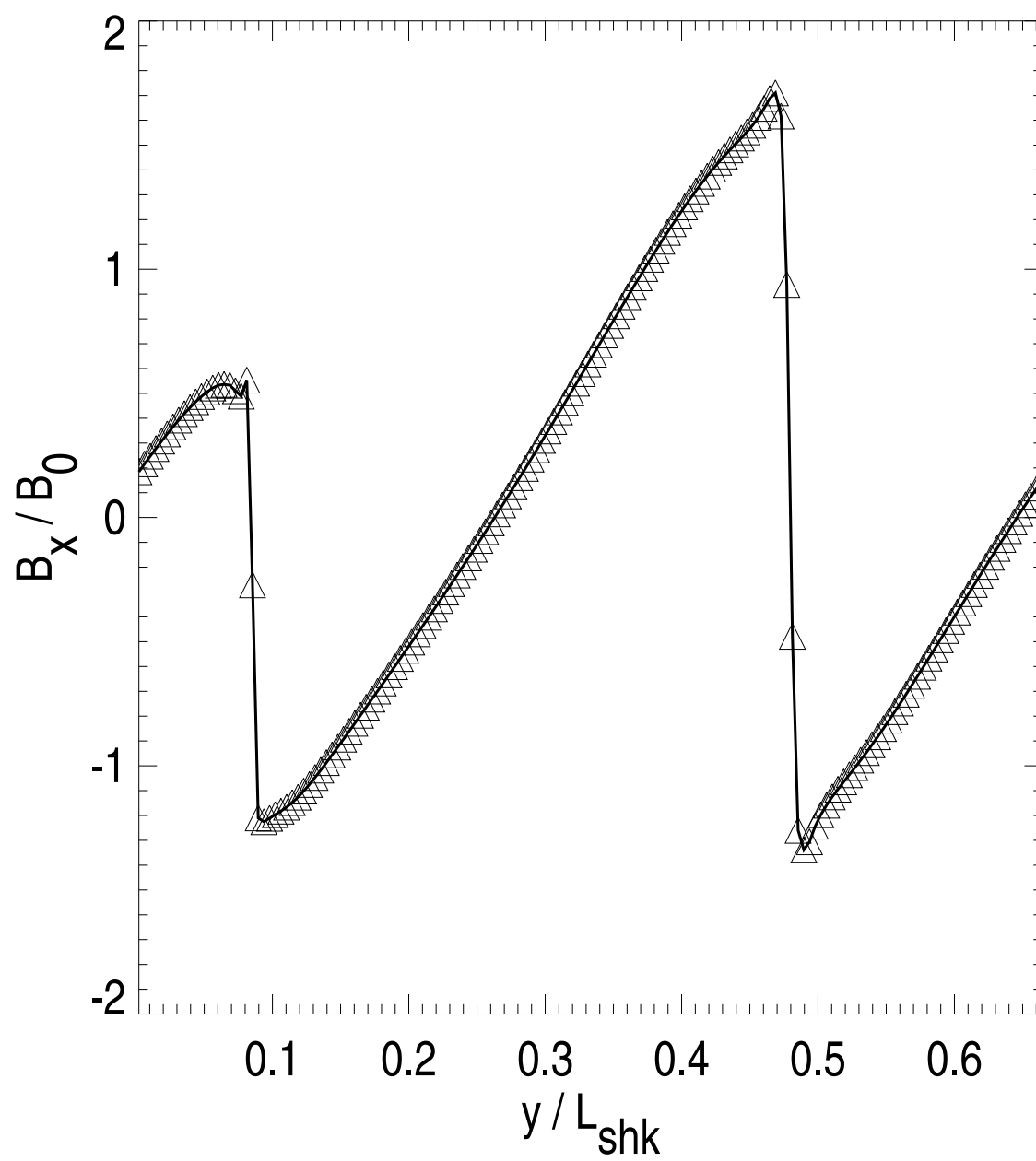
<http://arxiv.org/ps/astro-ph/9703172v1>

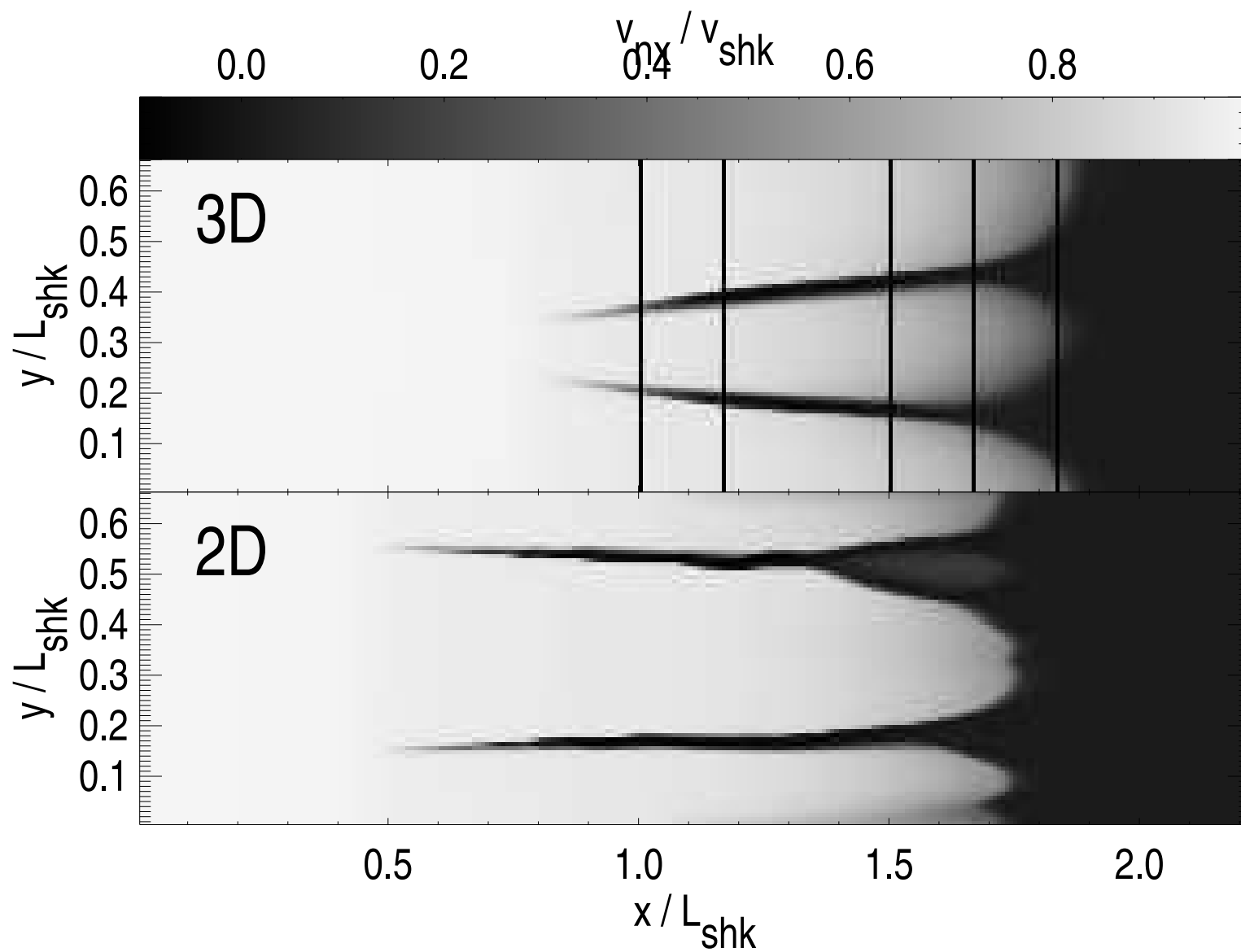


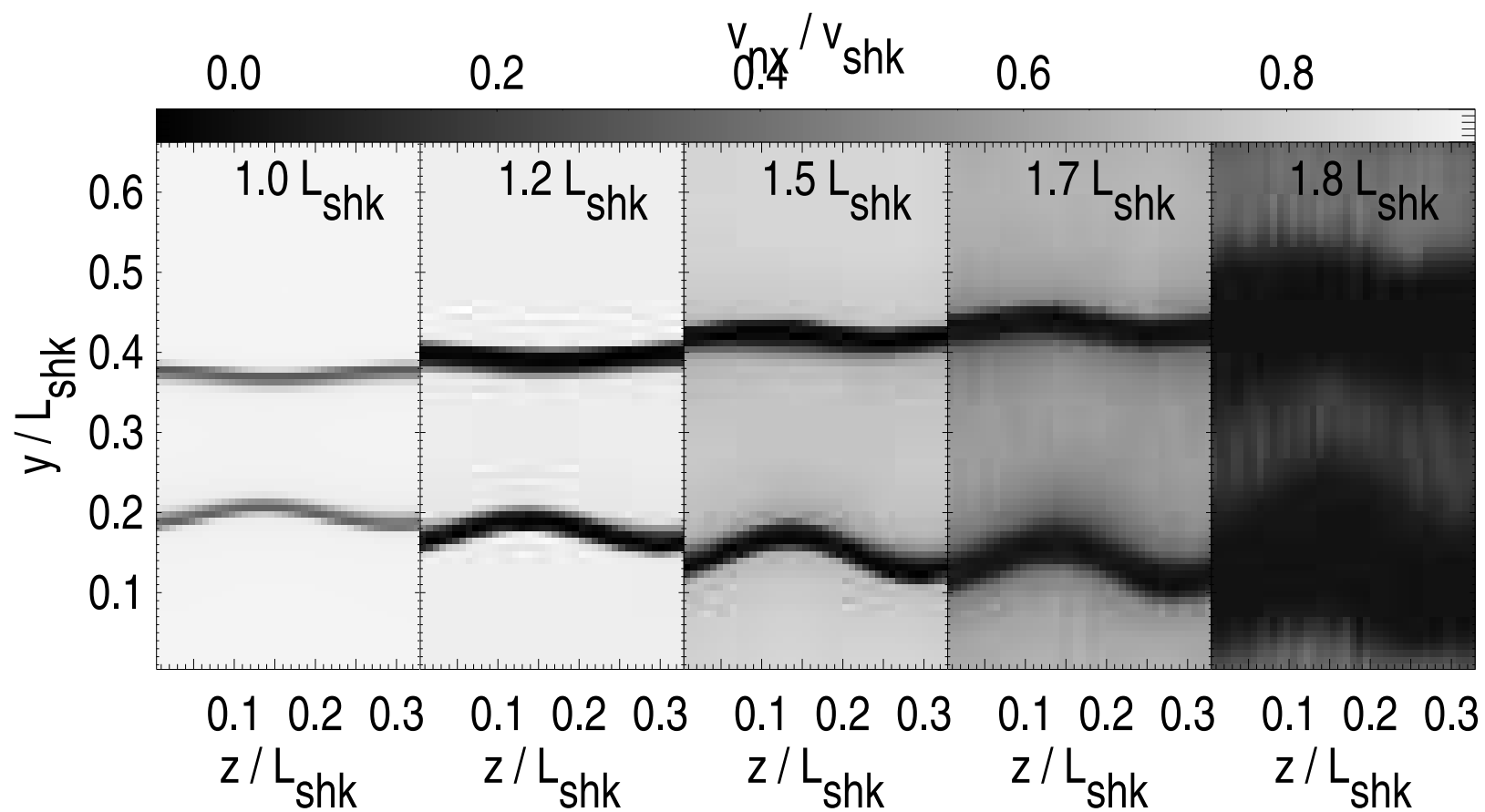


This figure "fig7.jpg" is available in "jpg" format from:

<http://arxiv.org/ps/astro-ph/9703172v1>

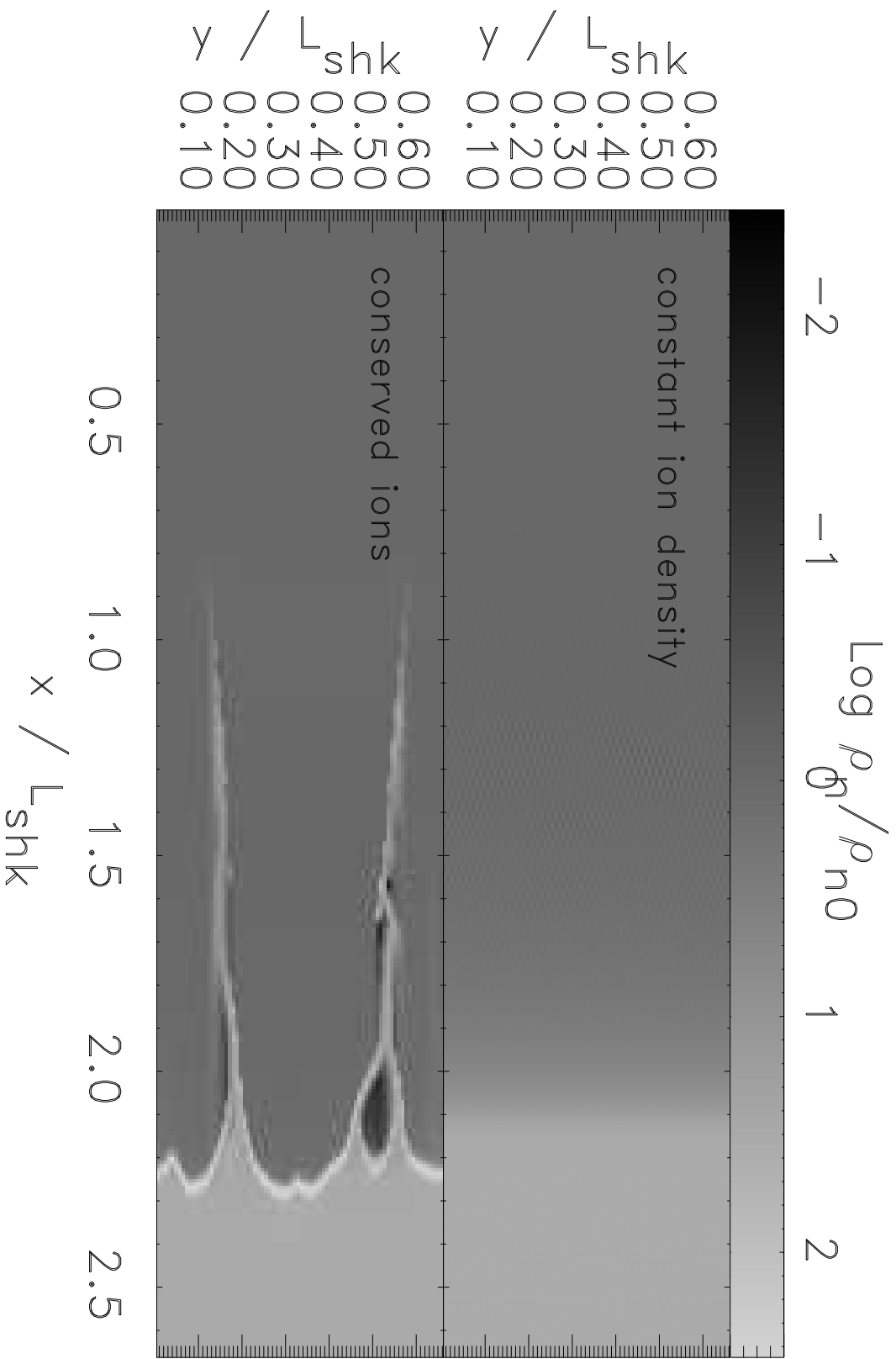






This figure "fig10.jpg" is available in "jpg" format from:

<http://arxiv.org/ps/astro-ph/9703172v1>



This figure "fig12.jpg" is available in "jpg" format from:

<http://arxiv.org/ps/astro-ph/9703172v1>

This figure "fig13a.jpg" is available in "jpg" format from:

<http://arxiv.org/ps/astro-ph/9703172v1>



This figure "fig13b.jpg" is available in "jpg" format from:

<http://arxiv.org/ps/astro-ph/9703172v1>

